JGR Atmospheres

RESEARCH ARTICLE
10.1029/2020JD033519

Key Points:

- The Lagrangian photochemical trajectory model is capable of tracking the sources of regional O_3 pollution at receptor site
- The North China Plain was the major origin of regional O_3 at Mt. Tai with an average contribution of 74 ± 27%
- Nocturnal O_3 at Mount Tai is a good indicator for predicting surface O_3 pollution over a wide spatial coverage

Supporting Information:

- Supporting Information S1
- Supporting Information S2

Correspondence to:
L. Xue,
xuelikun@sdu.edu.cn

Citation:
Zhang, Y., Xue, L., Li, H., Chen, T., Mu, J., Dong, C., et al. (2021). Source apportionment of regional ozone pollution observed at Mount Tai, North China: Application of Lagrangian photochemical trajectory model and implications for control policy. *Journal of Geophysical Research: Atmospheres*, *126*, e2020JD033519. https://doi.org/10.1029/2020JD033519

Received 14 JUL 2020
Accepted 5 DEC 2020

Source Apportionment of Regional Ozone Pollution Observed at Mount Tai, North China: Application of Lagrangian Photochemical Trajectory Model and Implications for Control Policy

Yingnan Zhang[1], Likun Xue[1,2,3], Hongyong Li[1], Tianshu Chen[1], Jiangshan Mu[1], Can Dong[1], Lei Sun[4], Hengde Liu[5], Yong Zhao[5], Di Wu[5], Xinfeng Wang[1], and Wenxing Wang[1]

[1]Environment Research Institute, Shandong University, Ji'nan, China, [2]Collaborative Innovation Center for Climate Change, Jiangsu Province, Nanjing, China, [3]Ji'nan Eco-Environmental Monitoring Center of Shandong Province, Ji'nan, China, [4]School of Environmental Science & Engineering, Qilu University of Technology (Shandong Academy of Sciences), Ji'nan, China, [5]Taishan National Reference Climatological Station, Tai'an, China

Abstract To better understand the characteristics and trace the sources of regional ozone (O_3) in the North China Plain (NCP), we analyzed 1-year continuous observations obtained at Mount Tai in 2018 and compared with previous data from 2006–2009. In the warm seasons (April–September), O_3 pollution (defined as a maximum daily 8-h average O_3 mixing ratio that exceeds 75 ppbv) occurred frequently (59%–92% of days) and O_3 concentrations significantly increased (especially in July–September) from 2006–2009 to 2018. We applied the Lagrangian photochemical trajectory model, built on the coupling of the Lagrangian backward trajectory model and Master Chemical Mechanism box model, to identify the source regions, key precursors, and emission sectors. The NCP was identified as the major source region with an average contribution of 74% ± 27% to the regional O_3 concentrations during the O_3 episodes in April–September. Regional O_3 formation was highly NOx-sensitive in air masses traveling from the southern part of the NCP but limited by anthropogenic hydrocarbons (especially alkenes) in air masses from the northern part of the NCP. The reduction of emissions from transportation and industry sectors would significantly reduce the regional O_3 concentrations. Biomass burning also exerts a significant influence on regional O_3 concentrations under certain circumstances. This study demonstrates that the regional background O_3 at mountaintop levels is a good indicator of surface O_3 pollution over a wide spatial coverage, and provides guidance for regional collaboration on emission control to mitigate photochemical air pollution over the NCP.

1. Introduction

Tropospheric ozone (O_3) is an important trace gas in the ambient air. The photolysis of O_3 in the troposphere provides an important primary source of the hydroxyl radical (OH), which initiates the chemical oxidation cycle (Lelieveld et al., 2008). Tropospheric O_3 serves as an important greenhouse gas that contributes to global warming (IPCC, 2013; Monks et al., 2015), and long-term exposure to high concentrations of surface O_3 is harmful to human health and vegetation (Fuhrer, 2009). Surface O_3 pollution has become a major environmental concern in China in recent decades (Wang, Xue, et al., 2017; and references therein; Xue, Wang, Gao, et al., 2014), and the increasing trends shown in several long-term studies provide evidence that the situation is worsening (Lu et al., 2018, 2020; Sun et al., 2016; Wang et al., 2019; Wang, Wei, Ding, et al, 2009; Xu et al., 2020). In contrast, the pollution by other routinely monitored pollutants (e.g., SO_2, NO_2, CO, $PM_{2.5}$, and PM_{10}) has significantly improved since 2013 (http://www.mee.gov.cn; Liu & Wang, 2020; Zheng et al., 2018). A clear understanding of the source apportionment of regional O_3 pollution is therefore critical for future air quality management in China.

In polluted urban areas, surface O_3 can be rapidly produced by photochemical reactions of volatile organic compounds (VOCs) and NOx (NOx = NO + NO_2). The O_3 can then be transported downwind to rural or remote areas and lead to regional O_3 pollution (Wang, Xue, et al., 2017; and references therein). The challenges of tracking regional O_3 pollution sources primarily exist in two aspects (Cooper et al., 2015; Schroeder et al., 2020). First, the formation mechanism of O_3 is complex and there is a highly nonlinear

relationship between O_3 and its precursors (VOCs and NOx), which poses difficulties for the accurate representation of O_3 formation using the chemical mechanisms in current models (Lyu et al., 2019; Xue, Wang, Gao, et al., 2014). The second challenge is the coupling of the regional transport and nonlinear chemistry between O_3 and its precursors (Xiao et al., 2010; Yang et al., 2019). For example, the O_3 in the receptor area may be sensitive to NOx (VOCs) locally and sensitive to VOCs (NOx) in the upwind areas. Decoupling of the regional transport and O_3-precursor relationship therefore presents a major challenge for current atmospheric research and air pollution control.

The North China Plain (NCP) is one of China's most rapidly developing regions and has experienced severe O_3 pollution in recent decades. Several studies have examined O_3 pollution characteristics, formation regimes, and source apportionment (Wang, Xue, et al., 2017; and references therein). In summer, high O_3 episodes (defined in this study as a maximum daily 8-h average O_3 mixing ratio (MDA8 O_3) that exceeds 75 ppbv) have occurred frequently in various environments covering urban, suburban, rural, and mountainous sites (Chen et al., 2020; Lyu et al., 2019; Ma et al., 2019; Sun et al., 2016; Wei et al., 2015; Zong et al., 2018). The maximum hourly O_3 concentration at a rural site downwind of Beijing reached as high as 286 ppbv in June–July 2005 (Wang et al., 2006) and long-term trend analyses have confirmed the rapid increase of regional O_3 concentrations (Sun et al, 2016, 2019; Xu et al., 2020). Many observation-based modeling studies have shown that O_3 formation in urban areas generally tended to be VOC-limited, whereas that in rural areas tended to be NOx-limited (Wang, Xue, et al., 2017). Some studies have also addressed O_3-precursor relationships over a large regional scale. Xing et al. (2011) examined the nonlinear response of O_3 to precursor emission reductions and found that regional sources were significant contributors to O_3 concentrations in Beijing and that the reduction of local emissions (even by 80%) in Beijing alone would be insufficient to resolve regional O_3 pollution. Xue, Wang, Louie, et al. (2014) also pointed out that increased regional transport negated the local control efforts in Hong Kong, southern China. These studies demonstrate the necessity of synchronous control on regional emissions over most areas of China.

Numerical models coupled with complex chemical mechanisms (especially zero-dimensional [0-D] and three-dimensional [3-D] models) have been widely used to track O_3 sources. Both model types have advantages and disadvantages. Specifically, 0-D models generally adopt detailed chemical mechanisms but only consider chemical processes, with little to no consideration of important physical processes, such as vertical and horizontal transport. As a result, 0-D models can reproduce the in situ chemistry of O_3 but their applications are largely limited by their small spatial representativeness (Chen et al., 2020; Ling et al., 2014; Lyu et al., 2016; Xue, Wang, Gao, et al., 2014). In comparison, 3-D models incorporate meteorological fields and can track O_3 sources at different spatial scales. Some source apportionment modules, such as Ozone Source Apportionment Technology, Decoupled Direct Method in three Dimensions, and Brute Force within 3-D air quality models, can provide detailed information on the source-receptor relationships of O_3 (Li et al., 2012; Xiao et al., 2010; Yang et al., 2019); however, their application tends to substantially increase the computational cost. As a result, 3-D models generally incorporate simplified chemical mechanisms as a compromise. In addition to 0-D and 3-D models, a photochemical trajectory model (PTM), which consists of a moving box of specific dimensions and detailed chemical mechanisms (e.g., Master Chemical Mechanism [MCM]), has been widely applied to describe regional-scale O_3 pollution in Europe (Derwent & Jenkin, 1991; Hough & Derwent, 1987). In this study, we improved the PTM construction as well as the physical and chemical modules, and built a Lagrangian PTM (LPTM) by coupling both a Lagrangian backward trajectory model (Draxler et al., 2018) and MCM box model (Jenkin et al., 2003; Saunders et al., 2003). The efficacy of the LPTM was verified by tracking regional O_3 sources on the premise of accurate decoupling of the regional transport and O_3-precursor relationship.

In this study, we analyzed the recent 1-year (2018) continuous observations of O_3 and related parameters at Mount Tai with a combination of LPTM simulations to better understand the causes of the severe regional O_3 pollution over the NCP. We first present the O_3 pollution characteristics observed in 2018 and compare with data from 2006 to 2009. We then track the origins of the O_3 precursors and quantify the contributions of different source regions to high regional O_3 concentrations using the LPTM. A series of sensitivity experiments were conducted to diagnose the key precursors and emission sectors over the major source regions. We also demonstrate the strong relationship between the regional O_3 background at mountaintop levels

and regional ground-level O_3 pollution, and make recommendations for regionally coordinated O_3 control strategies.

2. Materials and Methods

2.1. Observational Data Set

Field observations were conducted at the Taishan National Reference Climatological Station located on the summit of Mount Tai (36.26°N, 117.11°E) at an altitude of 1,534 m above sea level. Because of its high elevation, this site is rarely impacted by local anthropogenic emissions and data collected there well reflect regional O_3 pollution of the NCP. As a typical mountain site, Mount Tai is frequently influenced by the mountain-valley breezes. During the daytime, the valley breezes and evolution of the planetary boundary layer (PBL) bring the air pollutants from the valley to the mountaintop, while the air masses at nighttime are governed by the downslope transport and long-range transport of regional air in the free troposphere or the residual layer (Gao et al., 2005; Sun et al., 2016). Therefore, nocturnal O_3 data at Mount Tai were used to represent the regional background O_3 concentrations considering the small impact of NO titration on the mountaintop. This site is operated by Shandong University and continuously measures major trace gases and aerosol properties. In this study, we analyzed the 1-year continuous measurements from January 1, 2018 until December 31, 2018. Previous data collected from January 2006 to July 2009 were also analyzed for comparison to examine the decadal changes of regional O_3 concentrations (Sun et al., 2016).

Real-time measurements of trace gases, including O_3, NO, NO_2, NOy (NOy = NO + NO_2 + NO_3 + N_2O_5 + HONO + HNO_3 + NO_3^- + PANs + $RONO_2$ + etc.), and CO, were implemented using standard commercial techniques (Li et al., 2020). O_3 was measured by a model T400 UV photometric ozone analyzer (Teledyne Advanced Pollution Instrumentation (T-API)) with a detection limit of 0.4 ppbv and precision of 0.5%. NO and NOy were monitored using a chemiluminescence analyzer (model T200U, T-API) with a detection limit of 0.4 ppbv and precision of 0.5%. NOy was converted to NO by an externally placed molybdenum oxide converter prior to detection. NO_2 was monitored by an optical analyzer (model T500U, T-API) with a detection limit of 40 pptv and precision of 0.5%. CO was measured by gas filter correlation and non-dispersive infrared analyzers. From January 1, 2018 to July 30, 2018, CO was measured using a model 300 optical analyzer (T-API) with a detection limit of 50 ppbv and precision of 0.5%. From July 31, 2018 to December 31, 2018, CO was measured using a model T300U optical analyzer (T-API) with a detection limit of 20 ppbv and precision of 0.5%. During the measurements, these analyzers were routinely calibrated for the 1-year continuous observations in 2018. Multi-point calibrations were performed monthly and zero and span calibrations were performed weekly except for the CO analyzer. For CO, multi-point calibrations were performed monthly and the baseline was determined every 8 h by passing ambient air through the internal CO scrubber for 15 min. The calibration system and procedures have been described in detail by Li et al. (2020). Meteorological parameters including ambient temperature and relative humidity (RH) were obtained from the Taishan National Reference Climatological Station.

2.2. Lagrangian Photochemical Trajectory Model

Photochemistry during regional transport was reproduced using the LPTM, which was built based on the coupling of the Lagrangian backward trajectory model with the chemical box model. The LPTM consists of five major modules: input; initialization; physical; chemical; and output. The input module was called to read in the gridded emission rates of primary pollutants (non-methane VOCs [NMVOCs], NOx, CO, and SO_2) and meteorological parameters (temperature and RH). The initialization module was used to set the initial concentrations of major pollutants (O_3, NMVOCs, NOx, CO, and SO_2) and initialize the meteorological parameters (temperature, RH, and the PBL height). The physical and chemical modules incorporated complex physical and chemical processes, respectively. The output module outputted the selected species' concentrations and reaction rates. To provide a realistic description of the air exchange between air masses below the PBL and within the residual layers, the LPTM model was split into two layers vertically, with the upper layer describing the pollutant behavior within the residual layers and the lower layer receiving the ground-level primary emissions (Derwent & Jenkin, 1991). It should be noted that such a coarse vertical

resolution of model may inevitably introduce some uncertainties to the model representation of emissions and dilution mixing within the PBL.

The applied homogeneous chemical mechanism was the state-of-the-art MCM version 3.3.1 (MCMv3.3.1; http://mcm.leeds.ac.uk/MCM/; Jenkin et al., 2003; Saunders et al., 2003), which near-explicitly describes the reactions of 143 VOC species and has been widely used to reproduce the nonlinear chemistry between O_3 and its precursors in the atmosphere (Chen et al., 2020; Xue, Wang, Gao, et al., 2014). In addition to homogeneous chemistry, heterogeneous chemistry including N_2O_5 hydrolysis, HO_2 loss on aerosols, and HONO formation from NO_2 surface reactions were also considered in this model (Xue et al., 2016; Xue, Wang, Gao, et al., 2014). The heterogeneous chemical processes were disabled in this study. In addition to the complete chemistry, we also incorporated physical processes, including regional transport, solar radiation, diurnal evolution of the PBL, dry deposition, and air exchange between the air masses and residual layers. The regional transport was incorporated by backward trajectories. The solar radiation was calculated as a function of solar zenith angle under the assumption of clear sky conditions (Hayman, 1997). The PBL height was parameterized to rise linearly from the minimum height at 06:00 local time (LT) to the maximum height at 14:00 LT, remained constant at its maximum in the afternoon, and reduced to the minimum at 20:00 LT. The minimum and maximum heights were constrained using the data obtained by running the Hybrid Single-Particle Lagrangian Integrated Trajectory model (HYSPLIT, v4.9; Draxler et al., 2018). Dry deposition velocities of inorganic gases, peroxyacetyl nitrates, and oxygenated hydrocarbons were parameterized based on the work of Zhang et al. (2003). Air exchange between the air masses and residual layers only occurred when the PBL expanded in the morning, and the pollutant concentrations within the residual layers were set to the concentrations at 21:00 LT from the previous night (Derwent & Jenkin, 1991; Hough & Derwent, 1987). Dry deposition and air exchange between the air masses and residual layers were disabled when the trajectory was above the PBL. The major objective of this study is to quantify the contributions of O_3 precursor emissions and the O_3-precursor relationships from the specific source regions to the observed O_3 pollution at Mt. Tai with the LPTM. The potential impacts of transboundary transport from outside China and stratospheric intrusion were beyond the scope of this study and were not considered here.

We considered three types of primary emission sources: anthropogenic emissions; biogenic emissions; and biomass burning. The anthropogenic emissions (NMVOCs, NOx, CO, and SO_2) were derived from the MEIC inventory (Multi-resolution Emission Inventory for China; 0.25° × 0.25°; monthly resolution in 2016; http://www.meicmodel.org/; Li et al., 2014). The biogenic emissions (CO, isoprene, α-pinene, β-pinene, and limonene) were derived from the MEGANv2.1 inventory (https://bai.ess.uci.edu/megan/versions/megan21; 0.5° × 0.5°; monthly resolution in 2010; Sindelarova et al., 2014). The biomass burning emissions (NO, CO, SO_2, ethane, propane, ethyne, ethene, propene, benzene, toluene, formaldehyde, acetaldehyde, and Methyl ethyl ketone) were derived from Global Fire Emission Database (0.25° × 0.25°; monthly resolution in 2018; http://www.globalfiredata.org/; Akagi et al., 2011; Andreae & Merlet, 2001). These three inventories contain six principal emission sectors: power, industry, residential, transportation, biomass burning, and biogenic emissions. For biomass burning and biogenic emissions, the emission profile of contained individual NMVOC species was directly obtained from the corresponding inventories. For anthropogenic emissions, which represent the first four emission sectors, a ratio of 9:1 was used to allocate NOx into NO and NO_2. Besides, the emission profile of individual NMVOC species from a given anthropogenic emission sector was obtained from previous studies and the US Environmental Protection Agency (USEPA) SPECIATE 4.5 database (Li et al., 2014; Liu, Shao, Fu, et al, 2008; Liu, Shao, Lu, et al., 2008; Simon et al., 2010; Tsai et al., 2003; Wang, Wei, Du, et al., 2009; Yuan et al., 2010; Zheng et al., 2009). Table S1 presents the detailed fractional emissions of major NMVOC species from the different anthropogenic emission sectors. The overall emission rate (unit: molecules/cm^3/s) of each pollutant within a grid cell was calculated as follows. The species profile of each emission sector was first multiplied by its total emissions, the emission rate was then calculated assuming that the pollutants were well mixed within the PBL, and the emission rate of each pollutant was then summed from the above six emission sectors. The primary emissions from anthropogenic activities and biogenic sources were set to zero when the trajectory was above the PBL, and biomass burning emissions were assumed to be well mixed within 3,000 m.

Both single backward trajectories and clusters were obtained using the HYSPLIT model (v4.9; Draxler et al., 2018). In this study, a total of 103 3-D 3-day backward trajectories were computed once per day at the

time when hourly O_3 peak was observed on selected O_3 episode days (defined as when MDA8 O_3 exceeded 75 ppbv) during April–September 2018 with an ending point at an altitude of 300 m above ground level over Mount Tai. Four principal air mass clusters were determined using a built-in cluster analysis tool within the HYSPLIT model, and represented by their average transport trajectory. A detailed description of these four air mass clusters will be given in Section 3.2. The meteorological data used to drive the HYSPLIT model were provided by the Global Data Assimilation System (0.5°). Real-time meteorological parameters (temperature and RH) for the single backward trajectories were obtained along with the 103 backward trajectories, while for trajectory clusters meteorological parameters were obtained as averages of single backward trajectories included in each cluster.

The model only considered the emissions, photochemistry and transport of air pollutants in the regions fixed by the individual 3-day backward trajectories, while the processes outside these regions were not considered explicitly and only approximated by the initial concentrations of various pollutants in the model. As an air parcel traveled along a pre-defined trajectory, the initial concentrations of major pollutants were determined as follows. When the trajectory was below the PBL, O_3, NO_2, CO, and SO_2 were first initialized using the observational data obtained from the sites in the China's National Environmental Monitoring Center (CNEMC) Network, which are located nearest to the origin areas, and NO and NMVOCs were initialized using the data obtained from a typical urban site (Sun et al., 2018). When the trajectory was above the PBL, the initial concentrations of major pollutants were constrained using the regional background concentrations. For NMVOCs, the regional background concentrations were set using the data obtained from Mount Tai (Zhu et al., 2017). For other pollutants, the regional background concentrations in the NCP were determined using the observational data at Mount Tai, and those in other regions were obtained from previous studies (Wang, Xu, et al., 2017; Xing et al., 2017; Xu et al., 2020). Model simulations were then iteratively performed according to (E1) to make the model-simulated O_3 and related species be more reasonably consistent with the in-situ measurement data at Mount Tai:

$$CI_{i+1} = CI_i * \left(C_{\text{obs}} / CE_i\right) \tag{E1}$$

where CI_i and CE_i represent the initial and final concentrations of the target pollutant in the i^{th} simulation, respectively, and C_{obs} refers to the observed concentration of the target pollutant. Meteorological parameters, including temperature and RH, were initialized using the data obtained along with the backward trajectories. The maximum and minimum PBL heights obtained with the backward trajectories were also input into the model to calculate the real-time PBL heights.

For the model simulations, the meteorological parameters (temperature and RH) and emissions rates of major pollutants were read in with a time resolution of 1 h. These pollutants were then subjected to complex chemical reactions and physical processes. From the base model runs, we quantified the contributions from different source regions to the regional O_3 concentrations observed at Mount Tai on the 103 O_3 episode days during April–September 2018. In addition to the base runs, a series of sensitivity experiments were carried out to diagnose the formation regimes of the regional O_3 based on three classified major trajectory clusters, as described in Section 3.3. There were three major O_3 precursor groups, including NOx, anthropogenic hydrocarbons (AHC), and biogenic hydrocarbons (BHC). The AHC group was further sub-divided into low-reactivity hydrocarbons (LRHC, including ethane, propane, acetylene, and benzene), alkanes with carbon numbers ≥4 (C4HC), alkenes, and reactive aromatics (AROM; comprising most aromatics except for benzene). The detailed NMVOCs categorization is provided in Table S1.

3. Results and Discussion

3.1. O_3 Pollution Overview in 2018 and Comparison with 2006–2009

Figure 1 depicts the seasonal variations of surface O_3 at Mount Tai derived from the 1-year continuous observations in 2018. Overall, the O_3 exhibited a unimodal seasonality with a peak in June (85 ± 21 ppbv) and minimum in December (30 ± 8 ppbv). Further inspection shows that O_3 concentrations steadily increased from January to June and unevenly decreased from June to December. Specifically, O_3 concentrations were nearly constant in July–September and then sharply decreased from September to December. The factors

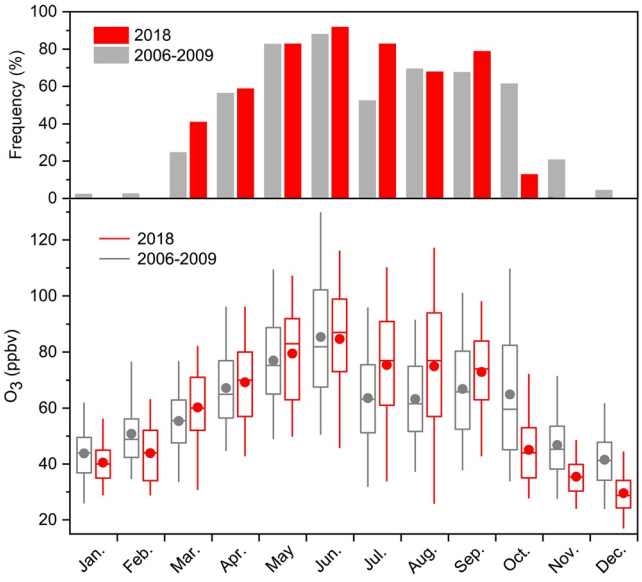

Figure 1. Seasonal variations of surface O_3 mixing ratios at Mount Tai during 2006–2009 and 2018. The box plot provides the 5%, 25%, 50%, 75% and 95% the data, while the dots indicate the average mixing ratios. The upper panel shows the frequency of the non-attainment days when MDA8 O_3 exceeded the Chinese National Ambient Air Quality Standard, that is, 75 ppbv (Class II). The previous data in 2006–2009 have been reported in Sun et al. (2016).

that shaped such a seasonal pattern of O_3 concentrations are elucidated as follows. The steadily increasing O_3 concentrations from January to June were affected by increasing temperatures and stronger photochemical activity, and the sharply decreasing O_3 concentrations from September to December were affected by decreasing temperatures and weakened photochemical activity. The frequent occurrence of stratosphere-to-troposphere exchange in April–May (as indicated by the observed high O_3 with low CO and RH in some cases) and strong biomass burning intensity in June also partly explain the high regional O_3 concentrations in these months (Chen et al., 2017; Tarasick et al., 2019). From June to July–August, the sharply decreasing O_3 concentrations were mainly due to the influence of strengthened Asia summer monsoon which decreased the intensity and frequency of stable anti-cyclonic synoptic weather circulation and brought more precipitation as indicated by the frequent cloudy days in July and August in Figure S1 (Ma et al., 2019; Zhang et al., 2016). The upper panel of Figure 1 shows the frequency of the O_3 episode days with MDA8 $O_3 \geq 75$ ppbv. Despite the high elevation and remote location, MDA8 O_3 non-attainment (exceedance) episodes occurred quite frequently at Mount Tai in the warm seasons, that is, April–September (59%–92% of days). In comparison, few non-attainment days were encountered in the cold seasons (October–March, 0%–41%). Hereafter, we focused on tracking the O_3 pollution sources in April–September.

Figure 2 presents the average diurnal variations of O_3, related species, and meteorological parameters in the warm and cold seasons. During both periods, major trace gases (O_3, NO, NO_2, NOy, and CO) showed well-defined diurnal cycles with a broad daytime concentration peak, which can be explained by the combined influence of PBL evolution, mountain–valley breeze, and atmospheric photochemistry (for O_3). The exact peak time

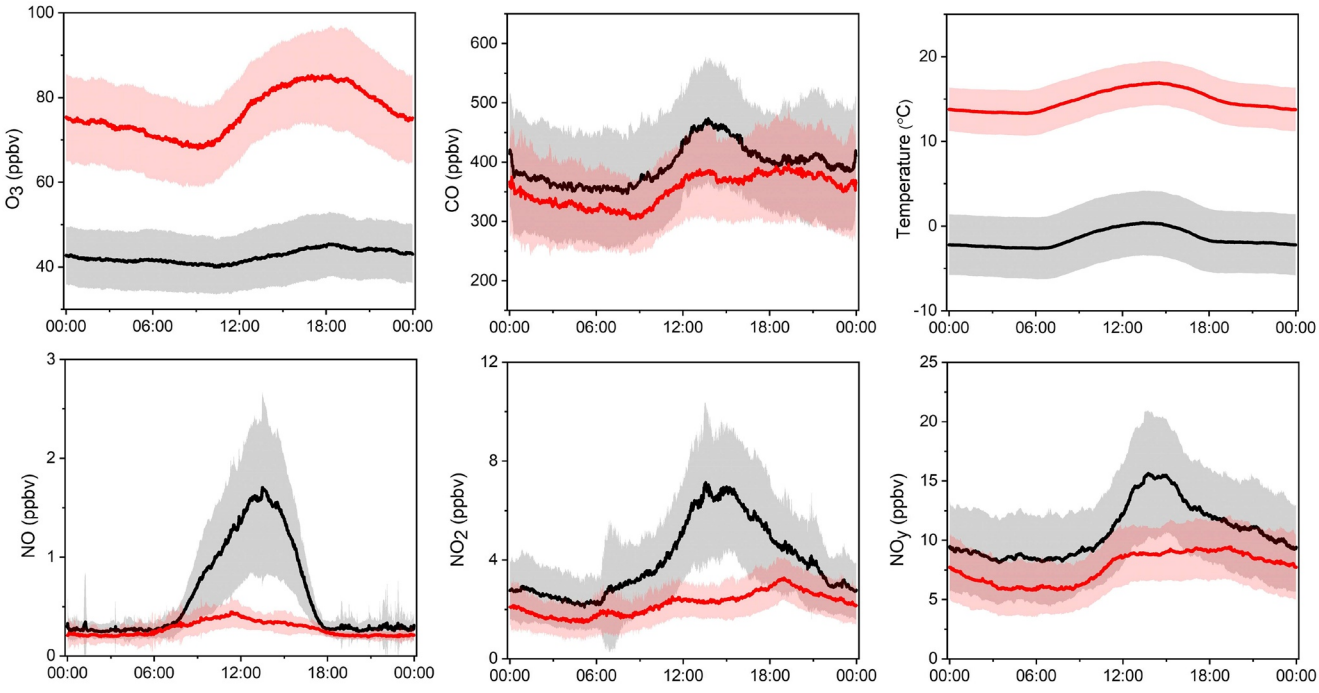

Figure 2. Average diurnal variations of O_3, related species, and meteorological parameters at Mount Tai during April–September (warm season; red) and October-March (cold season; black) 2018. Error bars indicate half standard deviation of the mean.

varied from pollutant to pollutant due to their different lifetimes and photochemical behaviors. Primary pollutants such as NO, NO_2, and CO exhibited higher concentrations in the cold seasons, whereas O_3 concentrations and ambient temperatures were substantially higher in the warm seasons. Two points are noteworthy here. First, higher regional background O_3 concentrations (calculated as the average value between 02:00 and 05:00 LT) were observed in the warm seasons (73 ± 20 ppbv) than in the cold seasons (42 ± 14 ppbv). Here we use the O_3 data during the hours of 2:00–5:00 LT to indicate regional background O_3 concentrations for two reasons, on one hand, Mount Tai is in the nocturnal residual layer and no local photochemistry occurs at nighttime, on the other hand, the NO titration effect was relatively weak during 2:00–5:00 LT (inferred from the diurnal variations of NO_2). Second, there was a larger enhancement (defined as the maximum minus the minimum) of the diurnal O_3 cycle in the warm seasons (38 ± 16 ppbv) than in the cold seasons (17 ± 8 ppbv), which indicates stronger photochemical ozone production in the warm seasons. These two factors together are responsible for the frequent MDA8 O_3 exceedance episodes in the warm seasons at Mount Tai.

The measurement results in 2018 and 2006–2009 are compared to demonstrate the decadal change of the regional O_3 concentrations (Figure 1), and one-way analysis of variance method (one-way ANOVA) was used to test the significance of the change. Compared with 2006–2009, the O_3 concentrations in 2018 were higher in the warm seasons (excluding June; $p < 0.01$) and lower in the cold seasons (excluding March; $p < 0.01$). The change in the warm-season O_3 is generally consistent with the increasing long-term O_3 trend (Li, Jacob, et al., 2019; Lu et al., 2018, 2020; Sun et al., 2016; Xu et al., 2020). We further selected July–October to examine the reasons responsible for such inter-annual variations considering both the severe O_3 pollution and large changes in O_3 concentrations during this period. For the meteorological parameters, higher temperatures and fewer cloudy days favored O_3 formation. We found that ambient temperature modestly increased in July (by 1.2 °C; $p < 0.01$) and August (by 1.7 °C; $p < 0.01$), slightly decreased in September (by −0.2°C; $p = 0.13$), and significantly decreased in October (by −2.5°C; $p < 0.01$) in 2018 compared with 2006–2009 (Figure S2). The significance of inter-annual variations of temperature was tested by one-way ANOVA. Cloudy days (i.e., with RH ≥ 95%) increased in July (by 17%), August (by 7%), and September (by 6%), but decreased in October (by −12%) (Figure S1). The temperature variations may partly explain the O_3 inter-annual variations in July, August, and October.

We selected a large regional domain scale (33–38°E, 115–120°N) to track the variations in abundance of the O_3 precursors based on the satellite retrievals (Figure S3). The data of tropospheric NO_2 column and vertical HCHO column were retrieved from the Ozone Monitoring Instrument (OMI; https://disc.gsfc.nasa.gov/. DOI:10.5067/Aura/OMI/DATA3007; DOI:10.5067/Aura/OMI/DATA3010). The amount of the tropospheric NO_2 column showed a significant decrease in July–September (by −10%, −30%, and −20%, respectively; $p < 0.01$) but showed an increase in October (by 14%; $p < 0.01$) in 2018 compared with 2006–2009. In contrast, the amount of the vertical HCHO column showed a significant increase in July–September (by 25%, 38%, and 17%, respectively; $p < 0.01$) and leveled off in October. The significance of inter-annual variations in the amount of tropospheric NO_2 column and vertical HCHO column was tested by one-way ANOVA. The consistent inter-annual variations of O_3 and HCHO abundance in July–September suggest that increasing VOCs is an important factor that enhances regional O_3 concentrations (Sun et al., 2016, 2019). We also examined the variations of other related factors. For example, the intensity of biomass burning activity declined in October, as indicated by a decrease in the number of fire spots within the selected domain scale (Figure S4). Overall, from 2006–2009 to 2018, the significant regional O_3 increase in July–September can be attributed to the elevated temperatures and increasing VOCs, and the sharp regional O_3 decrease in October can be attributed to the lower temperatures and weakened biomass burning intensity. Further observations are required to establish the long-term O_3 trends under the rapidly changing environment and climate in the NCP region.

3.2. Source Apportionment of O_3 Pollution

To identify the origins and transport patterns of the captured air masses, the three-dimensional 3-day backward trajectories for the 103 O_3 episode days were classified into four groups using a built-in cluster analysis tool within the HYSPLIT model. Figure 3 shows the four principal air mass clusters superimposed on the anthropogenic NMVOCs emissions. In the figure, “NEC” refers to the air masses from the north traveling over northeastern China; “EC” refers to the air masses from the southeast traveling over eastern China

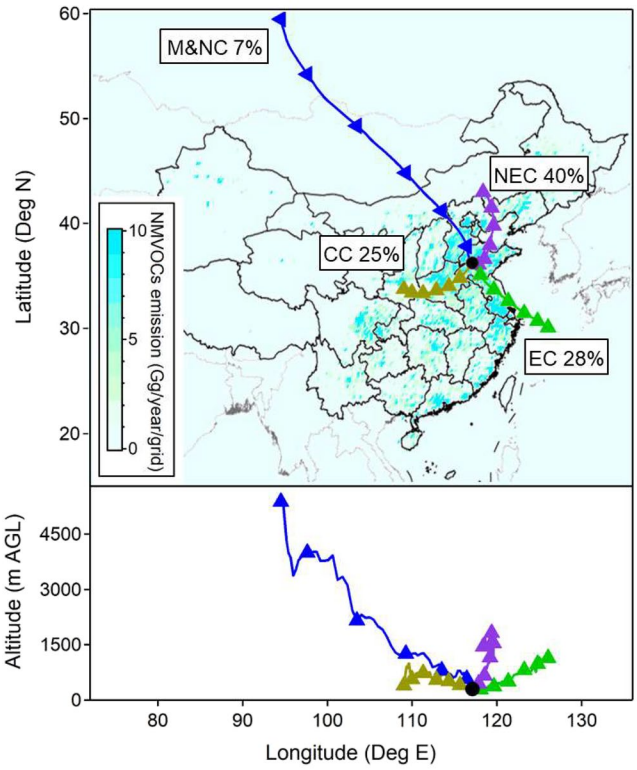

Figure 3. Principal air mass types and the 3-day backward trajectories arriving at Mount Tai during the 103 O_3 episodes in April-September 2018. The emission data of non-methane VOCs were taken from Li et al. (2017). Four principal air masses: (1) NEC: Northeast China, (2) EC: East China, (3) CC: Central China, and (4) M&NC: Mongolia and North China.

at low altitudes; "CC" refers to the air masses from the southwest traveling slowly over central China at low altitudes; and "M&NC" refers to the air masses from the northwest traveling quickly over Mongolia and northern China at relatively high altitudes. During the O_3 episodes in April–September, the NEC air mass occurred most frequently with a fraction of 40%, followed by EC (28%), CC (25%), and M&NC (7%); however, the dominant air masses varied between the different months (Table 1). The most frequent air mass was CC (56%) in April, which then changed to NEC (54%) in May. In June, NEC and EC were comparably frequent (35%), which then switched to EC (64%) in July. In August and September, the most frequent air mass again changed to NEC (67% and 55%, respectively). We also compared the summer transport pattern in 2018 with that in 2003–2015, and found that the EC air mass dominated in the summer during both periods. Such patterns in air mass transport are mainly attributed to the evolution of the Asian monsoon (Ding et al., 2008).

To further locate the origins of the O_3 precursors affecting Mount Tai, we present the spatial distributions of the NOx and NMVOC emission intensities along the 103 backward trajectories in Figure 4. The emission intensity of NOx and NMVOCs was calculated as the sum of the overall emission rate (Section 2.2) of the individual species. From a spatial perspective, there was a strong emission intensity within the NCP for both NOx and NMVOCs, which is consistent with previous studies that showed high NOx and NMVOC concentrations over the NCP (Li, Zhang, et al., 2019; Liu & Wang, 2020). This indicates that the O_3 pollution at Mount Tai was mainly influenced by O_3 precursor emissions in the NCP region. Few emissions were injected into the LPTM model outside of the NCP (with an exception of the Yangtze River Delta (YRD) in June–August) because most air masses moved at higher altitudes prior to approaching the NCP. On a temporal scale, the origins of the NOx and NMVOC emissions varied from month to month, which corresponds to the different dominant air masses. For example, NOx and NMVOCs were mainly from the southwestern part of the NCP in April, from the southeastern part of the NCP in June and July, and from the northern part of the NCP in May, August, and September (Figures S5 and S6). Overall, the NCP region was confirmed to be the major origin of the O3 precursors affecting Mount Tai.

Figure 5 compares the O_3, Ox, NOx, and CO results of the observations and LPTM simulations for the selected 103 O_3 episodes in April–September. The statistical measures used to evaluate the LPTM performance are documented in Table S2. The LPTM simulations showed generally reasonable agreement with the observations for most of the pollutants, as indicated by both the strong correlations (R^2: 0.41–0.81) and the reduced major axis (RMA) slopes (0.88–1.25). The results of statistical evaluation further confirmed the good performance of the LPTM, with mean fractional bias (MFB) and mean fractional error (MFE) meeting the benchmarks (MFB: 15%; MFE: 35%) recommended by the USEPA (2007). The model validation demonstrates that the LPTM is capable of reproducing the observations, which reflects a good representation of the emissions, chemistry, and physical processes. The good agreement also verifies the accuracy of the identified origins of the O_3 precursors, and provides a suitable method for quantifying the contributions of different source regions to the regional O_3 concentrations.

Table 1
Frequency of Major Air Mass Types Arriving at Mount Tai During the O_3 Episodes in April–September 2018

Type	April	May	June	July	August	September	April-September
NEC	25%	54%	35%	8%	67%	55%	40%
EC	0%	13%	35%	64%	33%	13.5%	28%
CC	56%	29%	30%	28%	0%	13.5%	25%
M&NC	19%	4%	0%	0%	0%	18%	7%

The contributions of the NCP and regions outside of the NCP to the regional O_3 concentrations observed at Mount Tai during the O_3 episodes in April–September were quantified based on the regional O_3 formation potential (ROFP). For a traveling aged air mass, the ROFP over a specific area is calculated by:

$$\mathrm{ROFP} = O_{3\mathrm{MAX}} - O_{3\mathrm{MIN}} \quad \text{(E2)}$$

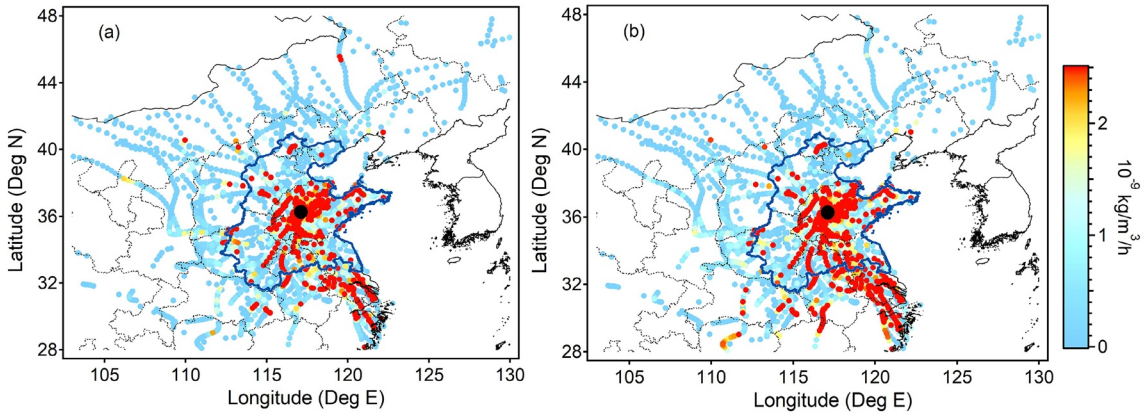

Figure 4. Spatial distributions of the (a) NOx and (b) NMVOC emission intensities along the 3-day backward trajectories arriving at Mount Tai during the O_3 episodes in April–September 2018. The areas inside the blue line refer to the domain of NCP region defined in this study.

where O_{3MAX} refers to the LPTM-simulated maximum hourly O_3 concentration on the last day (to guarantee that O_3 precursors have sufficiently undergone photochemical reactions) in the receptor area, and O_{3MIN} refers to the selected LPTM-simulated hourly minimum O_3 concentration that appeared prior to the O_{3MAX} in the receptor area. Such calculations reduce the uncertainties introduced by O_3 diurnal variations and can fully characterize the ongoing photochemical reactions over different source regions. As shown in Figure 6, the NCP was identified as a major source region to the LPTM-simulated regional O_3 concentrations

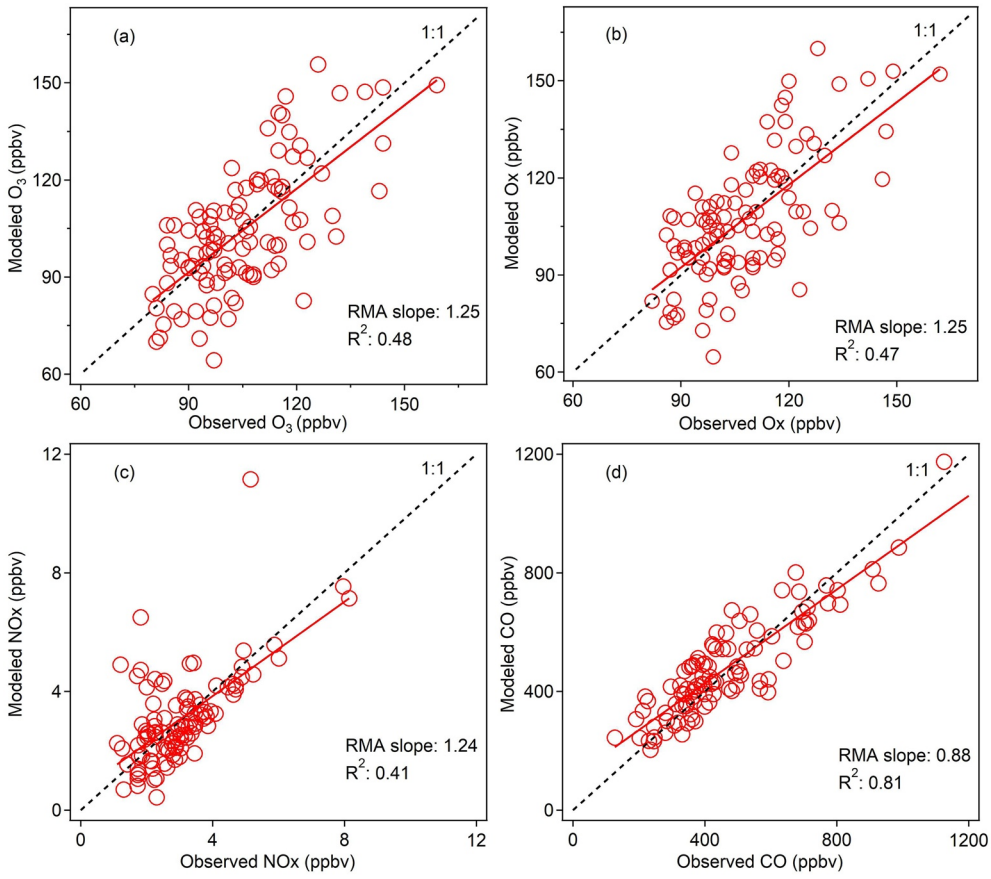

Figure 5. Comparison of (a) O_3, (b) Ox, (c) NOx, and (d) CO between field observations and LPTM simulations for the 103 O_3 episodes in April–September 2018. LPTM, Lagrangian photochemical trajectory model.

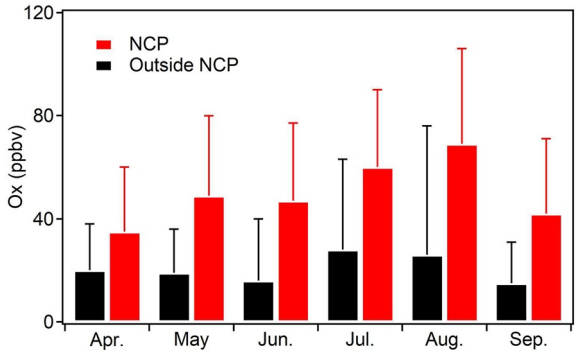

Figure 6. Contributions (calculated based on Regional O_3 Formation Potential [ROFP]) of NCP and regions outside NCP to the LPTM-simulated O_X concentrations at Mount Tai during the O_3 episodes in April-September 2018. Error bars indicate standard deviation of the mean. LPTM, Lagrangian photochemical trajectory model; NCP, North China Plain.

with an average contribution of 74% ± 27%, which further confirms that O_3 pollution observed at Mount Tai is regionally representative. The Ox ($Ox = O_3 + NO_2$) data were used in the calculations to eliminate the effect of NO titration. A notable point of these results is the high simulated O_3 concentrations in July and August. On one hand, this finding reveals rapid O_3 production in July and August due to high temperatures and abundant precursors. On the other hand, the high simulated O_3 concentrations in these two months should be related to the LPTM's overestimation due to the lack of rain deposition in the model. Corresponding to the NOx and NMVOCs emission origins, the regional O_3 concentrations were mainly contributed by the southwestern part of the NCP in April, by the southeastern part of the NCP in June and July, and by the northern part of the NCP in May, August, and September.

3.3. Sensitivity of Regional O_3 Pollution to Coordinated Reduction of O_3 Precursors

We examined the formation regimes of regional O_3 for the major air mass clusters NEC, EC, and CC based on a metric of relative incremental reactivity (RIR) (M&NC was not considered due to the low frequency and high elevation). RIR is defined here as the ratio of the percent decrease in the LPTM-simulated regional O_3 concentrations to the percent decrease in the emissions of the target O_3 precursor group over a specific source region. Figure 7 shows the RIRs for the different O_3 precursor groups in designated regions: "Local" refers to Ji'nan and Tai'an (the closest cities surrounding Mount Tai); "NCP" refers to the other areas over the NCP (Figure 4) excluding Ji'nan and Tai'an; and "Outside NCP" refers to areas excluding Local and NCP. Overall, the regional O_3 formation was most sensitive to emission reductions over the NCP for all three air mass clusters, which is consistent with the source apportionment results in Section 3.2. We therefore focused on the emission reductions in the NCP region in the following analyses.

As shown in Figure 7, the key precursors varied among the three major air mass clusters as they traveled over different areas and thus have different NOx and NMVOC emission characteristics. For air masses traveling over the northern part of the NCP (i.e., NEC), regional O_3 formation was highly sensitive to AHC,

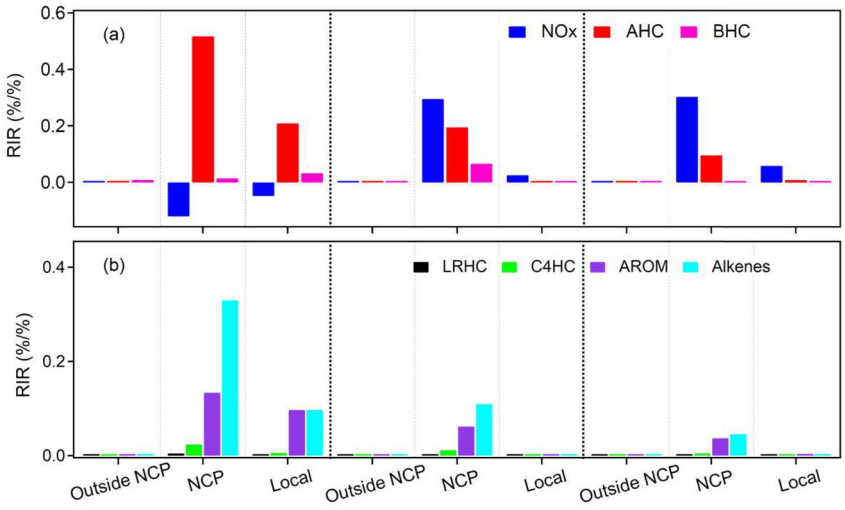

Figure 7. The LPTM-calculated RIRs for (a) major O_3 precursor groups and (b) the AHC sub-groups over different source regions among major air mass clusters. The left, middle, and right panel divided by the black dotted line was for major air mass types NEC, EC, and CC, respectively. Three major source regions: (1) Local: Tai'an and Ji'nan, (2) NCP: The areas covered in the blue line in Figure 4 excluding Tai'an and Ji'nan, (3) Outside NCP: The areas excluding Local and NCP. Refer to Table S1 for the detailed speciation of LRHC, C4HC, AROM, and alkenes. LPTM, Lagrangian photochemical trajectory model; NCP, North China Plain; RIR, relative incremental reactivity.

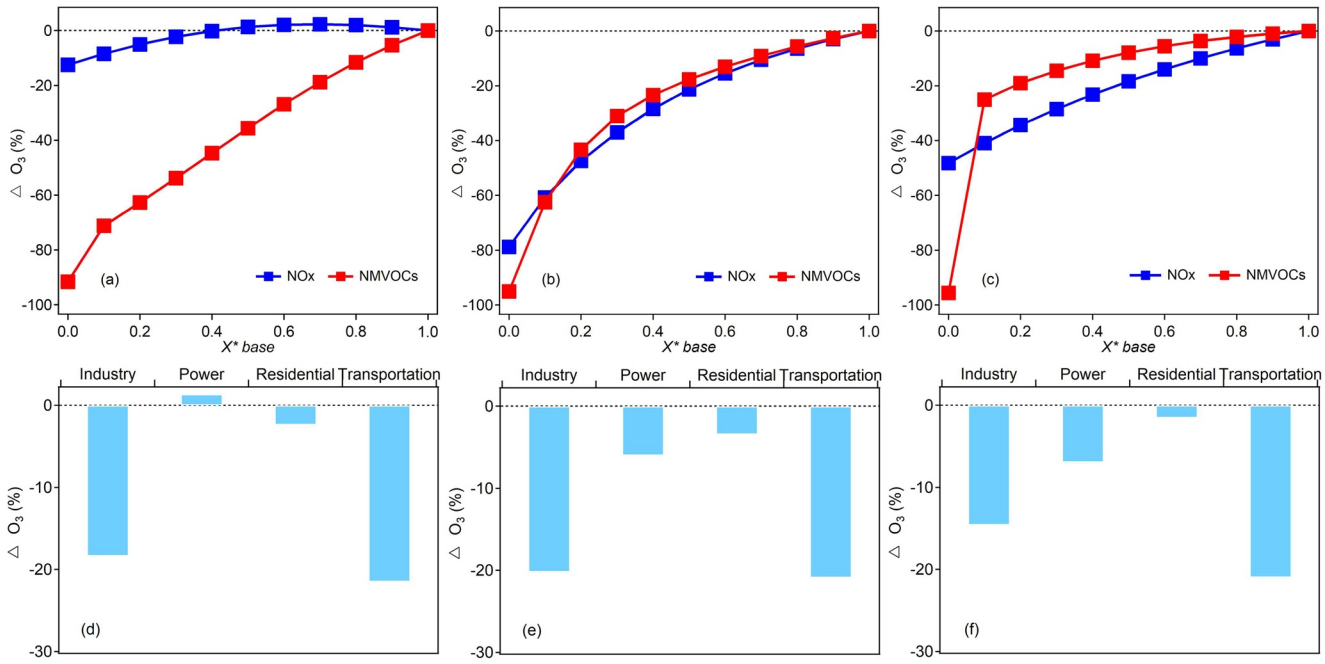

Figure 8. The LPTM-simulated regional O_3 change (a–c) as a function of the X times of the base emission intensity of NO_2 and NMVOCs and (d–f) as a result of shutting off major emission sectors over the NCP region. The left, middle, and right panel was for major air mass types NEC, EC, and CC, respectively. LPTM, Lagrangian photochemical trajectory model; NCP, North China Plain.

which was dominated by alkenes followed by reactive aromatics (Figure 7b). The RIRs for NOx were negative. Examination of detailed air mass trajectory and the associated anthropogenic emissions revealed that the NEC air masses had traveled in a highly polluted region with more intense NOx emissions prior to arriving at Mt. Tai. Thus, the NEC air masses contained higher levels of NOx compared to the EC and CC air masses and the O_3 formation was in a NOx-saturated regime during the transport over the NCP region. A small amount of NOx reduction would lead to less NO titration and higher regional O_3 concentrations. We further examined the effects of precursor reduction with different ratios over the NCP on regional O_3 concentrations (Figure 8a) and found that the control of NOx emissions only contributed to a regional decrease of O_3 when the reduction ratios exceeded 50%. Along similar reduction scales, the control of NMVOCs was consistently and significantly superior to NOx control for improving the regional O_3 pollution. Figure 8b shows the effects of shutting off major emission sectors over the NCP on the regional O_3 concentrations. For the NEC air mass, control priority should be given to the transportation and industry emission sectors, which reduced the regional O_3 concentrations by −22% and −18%, respectively, whereas the control of residential emissions showed little impact (−2%). In fact, shutting off the power sector alone even caused a slight increase (1%) in regional O_3 concentrations due to the high NOx emissions.

For air masses traveling over the southern part of the NCP (i.e., EC and CC), regional O_3 formation was most sensitive to NOx and to a lesser extent AHC (alkenes and reactive aromatics are key compounds) at 10% reductions. However, when shutting off the primary emissions over the NCP (i.e., 100% reductions), regional O_3 formation showed a larger dependence on AHC. The turnover was caused by the substantially slower radical cycling with 100% NMVOC reductions, which further affected NOx cycling and significantly limited O_3 formation. BHC showed relatively higher RIR (0.07) in the EC than in the NEC (0.01) and CC (0.001). Similar to the NEC results, controlling transportation and industry emissions would significantly reduce regional O_3 concentrations (by −21% and −20% for EC, respectively, and by −21% and −15% for CC), whereas controlling residential emissions showed little impact (reductions by −3% for EC and −2% for CC). The effect of shutting off power emissions resulted in a modest decrease (by −6% for EC and −7% for CC) of the regional O_3 concentrations. These results elucidate the different O_3 formation regimes among the three major air mass clusters and provide detailed information on the O_3-precursor relationships along the regional transport of aged air masses to Mount Tai.

Previous studies have reported the significant impacts of biomass burning on regional air quality over the NCP in June, the winter-wheat harvest season in northern China (Chen et al., 2017; Gu et al., 2020). In this study, we focused on the impact of biomass burning on regional O_3 concentrations. To elucidate the impact, we selected three typical cases with 3-day backward trajectories that had traveled over areas with intense fire spots and been injected into comparatively large biomass burning emissions, as shown in Figures S7 and S8. The 3-day backward trajectories of cases (a) and (b) came from eastern China and were classified into type EC. For case (a)/(b), the observed maximum O_3 concentrations were 113/114 ppbv, and the simultaneously observed concentrations of NOx and CO were 3.25/2.05 ppbv and 433/376 ppbv, respectively. Shutting off biomass burning emissions caused an −8% and −5% decrease in the LPTM–simulated regional O_3 concentrations over the receptor site. For case (c), the 3-day backward trajectory came from northeastern China and was classified into type NEC. The observed maximum concentration of O_3 (98 ppbv) and simultaneously observed concentration of CO (356 ppbv) were lower than the former two cases, but the simultaneously observed NOx concentrations (4.70 ppbv) were higher. Shutting off biomass burning emissions caused an −11% decrease in the LPTM–simulated regional O_3 concentrations over the receptor site. Further inspection of the time series (Figure S7) and 3-day backward trajectories (Figure S8) clearly showed that the decreased regional O_3 concentrations in these three cases were mainly caused by reduced biomass burning emissions from the NCP. These results suggest that biomass burning remains an important emission source over the NCP under certain circumstances and should be given attention in future control measures.

Jian and Fu (2014) showed that the retrieved smoke pixel heights ranged from 0 to 6 km above the local terrain over peninsular Southeast Asia, and 55% of the smoke pixels were below 1 km. Here we chose a median value of 3 km as biomass-burning smoke plume height (named as "BASE" scenarios) and conducted a series of sensitivity tests in June by assuming that biomass burning emissions were well mixed within 1 km (named as "ADJ" scenarios). The uncertainties introduced by biomass burning emission treatment were evaluated from three aspects. First, there is a negligible impact on the change in LPTM-simulated O_3 mixing ratios for the 17 O_3 episodes in June (<3%; $R^2 = 0.81$); Second, the NCP was identified as a dominant source region to the LPTM-simulated regional O_3 concentrations under both scenarios (with an average contribution of 74% and 78% under "BASE" and "ADJ" scenarios, respectively); Third, under "ADJ" scenarios, shutting down the biomass burning emissions resulted in decreases of −13%, −9%, and −18% in the LPTM–simulated regional O_3 concentrations over the receptor site for case (a), (b), and (c), respectively. Overall, the results indicated that the impacts of model treatment of biomass burning emissions on major conclusions should be minor.

3.4. Implications for Control Policy

Surface O_3 pollution over the NCP in summer is among the most severe worldwide, as indicated by studies within the Tropospheric Ozone Assessment Report (Cooper et al., 2020; Fleming et al., 2018; Gaudel et al., 2018; Lefohn et al., 2018; Xu et al., 2020). The long-term increasing trend of surface O_3 concentrations and regional background O_3 concentrations implies a worsening prospect of regional O_3 pollution, as well as the strong interplay between them (Sun et al., 2016; Xu et al., 2020). In Sections 3.2 and 3.3, we showed the significant impacts of ground-level emissions to high-elevation O_3 concentrations. In this section, we focus on the implications of high-elevation O_3 on ground-level O_3 pollution. Previous studies have reported that the downward transport of high-elevation O_3 would aggravate ground-level O_3 pollution to a certain degree (Zhu et al., 2020). Here we used the nocturnal averages of ambient O_3 concentrations (between 02:00 and 05:00 LT) observed at Mount Tai to represent regional background O_3 concentrations, and further examined to what spatial scales the regional background O_3 observed at Mount Tai can offer accurate indications for the next day's ground-level O_3 pollution.

We calculated the MDA8 O_3 concentrations of 24 selected cities (Figure S9) around Mount Tai and performed correlation analyses with the regional background O_3 observed at Mount Tai (Figure 9a). The 24 selected cities cover most areas of the NCP, and all (excluding Tai'an) are identified as key cities of the air pollution transport channel in Jing-Jin-Ji (a total of 28 cities whose air pollution have high potential to affect the air quality in Beijing and the whole Jing-Jin-Ji region; http://www.mee.gov.cn/). The MDA8 O_3 of the individual cities was calculated using the MDA8 O_3 averages of all of sites in the CNEMC inside each city. There were significant positive correlations between the regional background O_3 and ground-level

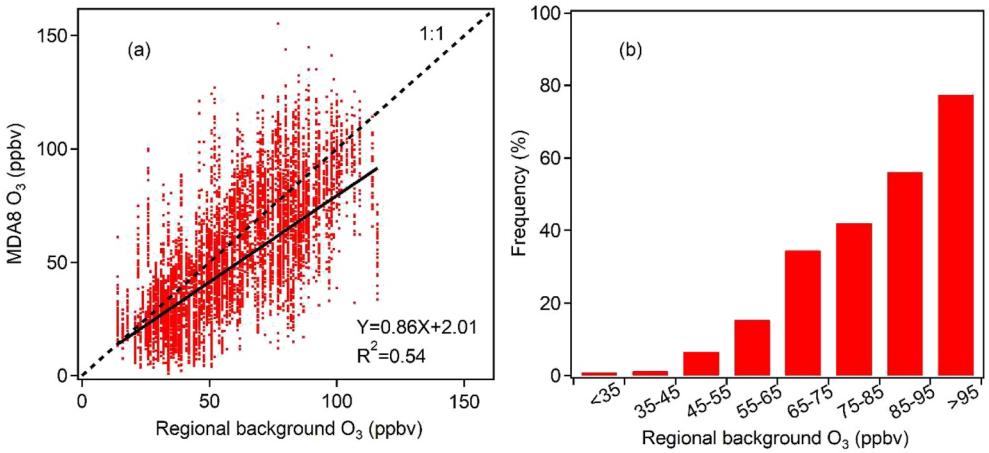

Figure 9. (a) Scatter plots of the MDA8 O_3 concentrations in 24 surrounding cities (see the detailed information in Figure S9) versus nocturnal regional background O_3 concentrations observed at Mount Tai; (b) The frequency of the non-attainment days when MDA8 O_3 of 24 surrounding cities exceeded the Chinese National Ambient Air Quality Standard (i.e., 75 ppbv [Class II]) versus different ranges of regional background O_3 concentrations. Regional background O_3 concentrations were obtained using the ambient O_3 averages observed at Mount Tai between 02:00 and 05:00 LT. The MDA8 O_3 of the individual cities was calculated using the MDA8 O_3 averages of all of sites in the China's National Environmental Monitoring Center (CNEMC) Network inside each city.

MDA8 O_3 (R^2: 0.54; slope: 0.86). The detailed correlation analysis results of individual cities are presented in Figure S10. There was a decreasing slope tendency (ranging from 0.99 to 0.76) and R^2 (ranging from 0.65 to 0.44) with increasing distance from Mount Tai, and the largest slope and R^2 were found in Ji'nan and Tai'an, respectively, which are the closest cities to Mount Tai. We also calculated the MDA8 O_3 non-attainment frequency of all 24 cities corresponding to the different ranges of regional background O_3 (Figure 9b). The MDA8 O_3 non-attainment frequency increased steadily with increasing regional background O_3. When the regional background O_3 concentration was less than 35 ppbv, the MDA8 O_3 non-attainment frequency was small (<1% of days), but when it exceeded 55 ppbv, the MDA8 O_3 non-attainment frequency of the 24 surrounding cities rapidly increased (by 16% ± 6% on average for each 10-ppbv increase of regional background O_3 concentrations ranging from 55 to 95 ppbv), and the MDA8 O_3 non-attainment frequency of the 24 surrounding cities exceeded 50% when the regional background O_3 concentration was higher than 85 ppbv. There was also a decreasing tendency of the MDA8 O_3 non-attainment frequency with increasing distance from Mount Tai (Figure S10). These results suggest that regional background O_3 is a good indicator for forecasting ground-level O_3 pollution over a relatively large spatial scale. For comparison, we performed similar analyses but used the O_3 data observed at Mount Tai during 0:00–5:00 and 0:00–6:00 LT to represent regional background O_3 concentrations, and the results showed little impacts on our major conclusions.

In this study, we traced the sources of regional O_3 pollution over the NCP based on data observed at the summit of Mount Tai, examined the sensitivity of regional O_3 pollution to coordinated precursor reduction, and further revealed the satisfactory ability of regional background O_3 to indicate ground-level O_3 pollution. Based on these results, we provide the following suggestions for future control of surface O_3 pollution. First, nocturnal O_3 observed at Mount Tai is a good indicator for ground-level O_3 pollution over a wide spatial coverage. Second, the NCP itself serves as the major source region for both precursor and regional O_3 concentrations. Improving the severe surface O_3 pollution would require synchronous reductions of regionally emitted precursors. Lastly, we suggest that different emission reduction measures should be implemented over different domains to better control surface O_3 pollution. Specifically, the northern part of the NCP should reduce NMVOC emissions while the southern part of the NCP should place emphasis on NOx reductions. From the perspective of specific emission sectors, control policy should give priority to the transportation and industry emission sectors.

4. Conclusions

We analyzed the year-round O_3 observations obtained at Mount Tai, northern China, in 2018. The frequent occurrence of MDA8 O_3 non-attainment episodes (59%–92% of days) revealed the severe regional O_3 pollution in the NCP region in the warm seasons. Well-defined diurnal cycles of major trace gases with a broad daytime concentration peak elucidated the important contributions of regional transport. From 2006–2009 to 2018, O_3 concentrations showed a significant enhancement in July–September due to elevated temperatures and increasing VOCs, but sharply declined in October due to lower temperatures and weakened biomass burning intensity. The magnitude and pattern of observed O_3 and related trace gases were well reproduced by the Lagrangian photochemical trajectory model. Further inspection of the model results suggested that the NCP is responsible for both the precursors and high regional O_3 concentrations (with an average contribution of 74% ± 27%) observed at Mount Tai during the O_3 episodes in April–September. Regional O_3 formation was highly NOx-sensitive in air masses traveling from the southern part of the NCP and AHC-sensitive in air masses from the northern part of the NCP. Key species within the AHC group were alkenes followed by aromatics. Control policy should give priority to the transportation and industry emission sectors considering their significance to reducing regional O_3 concentrations. Biomass burning was also found to make an important contribution to regional O_3 concentrations under certain circumstances. This study reveals that the regional background O_3 observed at the studied mountaintop provides a good indication of the surface O_3 pollution over a wide spatial coverage, and provides scientific support for the formulation of regional collaborative control policies to mitigate photochemical air pollution in the NCP region.

Although the efficacy of the LPTM has been confirmed by the reasonable agreement between model simulations and field observations, it is indeed subject to some uncertainties, mainly because of the lack of more refined trajectories and emission inventories as well as the relatively coarse spatial resolutions of the model. More efforts are still required to further enhance the LPTM's performance. The following directions are recommended for the future study: (1) the air mass trajectory with higher spatial resolutions is in great demand to better resolve the regional transport from upwind areas and local dynamics around the receptor area; (2) weather conditions such as cloud fraction and rainy days over traveling areas would significantly influence photolysis rate of pollutants, therefore, parameterizations of these processes in the model are of great importance; and (3) the emission inventories with higher temporal and spatial resolutions and detailed NMVOC emission profile are highly needed to reduce the uncertainty related to primary emissions.

Acknowledgments
We thank the University of Leeds for providing the Master Chemical Mechanism (version 3.3.1), the NOAA Air Resources Laboratory for providing the HYSPLIT model, and the NASA Goddard Earth Sciences Data and Information Services Center (GES DISC) for the free distribution of the OMI satellite data through the website (https://disc.gsfc.nasa.gov/). We also thank the Tsinghua University for providing the MEIC emission inventory, and the University of California, Irvine for providing the biogenic emission inventory. This work was funded by the National Natural Science Foundation of China (41922051), Shandong Provincial Science Foundation for Distinguished Young Scholars (ZR2019JQ09), National Key Research and Development Program of China (2016YFC0200500), and the Jiangsu Collaborative Innovation Center for Climate Change. We appreciate the two anonymous reviewers for their helpful suggestions to improve the original manuscript.

Data Availability Statement

Data associated with this study are accessible at http://dx.doi.org/10.17632/hjkbkkktsc.1.

References

Akagi, S. K., Yokelson, R. J., Wiedinmyer, C., Alvarado, M. J., Reid, J. S., Karl, T., et al. (2011). Emission factors for open and domestic biomass burning for use in atmospheric models. *Atmospheric Chemistry and Physics*, *11*(9), 4039–4072. https://doi.org/10.5194/acp-11-4039-2011

Andreae, M. O., & Merlet, P. (2001). Emission of trace gases and aerosols from biomass burning. *Global Biogeochemical Cycles*, *15*(4), 955–966. https://doi.org/10.1029/2000gb001382

Chen, J., Li, C., Ristovski, Z., Milic, A., Gu, Y., Islam, M. S., et al. (2017). A review of biomass burning: Emissions and impacts on air quality, health and climate in China. *The Science of the Total Environment*, *579*, 1000–1034. https://doi.org/10.1016/j.scitotenv.2016.11.025

Chen, T., Xue, L., Zheng, P., Zhang, Y., Liu, Y., Sun, J., et al. (2020). Volatile organic compounds and ozone air pollution in an oil production region in northern China. *Atmospheric Chemistry and Physics*, *20*, 7069–7086. https://doi.org/10.5194/acp-20-7069-2020

Cooper, O. R., Langford, A. O., Parrish, D. D., & Fahey, D. W. (2015). Challenges of a lowered U.S. ozone standard. *Science*, *348*(6239), 1096–1097. https://doi.org/10.1126/science.aaa5748

Cooper, O. R., Schultz, M. G., Schroder, S., Chang, K. L., Gaudel, A., Benitez, G. C., et al. (2020). Multi-decadal surface ozone trends at globally distributed remote locations. *Elementa: Science of the Anthropocene*, *8*, 23. https://doi.org/10.1525/elementa.420

Derwent, R. G., & Jenkin, M. E. (1991). Hydrocarbons and the long-range transport of ozone and pan across Europe. *Atmospheric Environment*, *25*(8), 1661–1678. https://doi.org/10.1016/0960-1686(91)90025-3

Ding, A. J., Wang, T., Thouret, V., Cammas, J. P., & Nédélec, P. (2008). Tropospheric ozone climatology over Beijing: Analysis of aircraft data from the MOZAIC program. *Atmospheric Chemistry and Physics*, *8*(1), 1–13. https://doi.org/10.5194/acp-8-1-2008

Draxler, R., Stunder, B., Rolph, G., Stein, A., & Taylor, A. (2018). *HYSPLIT4 USER's GUIDE version 4—Last revision: February 2018*. Retrieved from https://www.arl.noaa.gov/documents/reports/hysplit_user_guide.pdf

Fleming, Z. L., Doherty, R. M., von Schneidemesser, E., Malley, C. S., Cooper, O. R., Pinto, J. P., et al. (2018). Tropospheric Ozone Assessment Report: Present-day ozone distribution and trends relevant to human health. *Elementa: Science of the Anthropocene*, *6*, 12. https://doi.org/10.1525/elementa.273

Fuhrer, J. (2009). Ozone risk for crops and pastures in present and future climates. *Naturwissenschaften*, *96*(2), 173–194. https://doi.org/10.1007/s00114-008-0468-7

Gao, J., Wang, T., Ding, A., & Liu, C. (2005). Observational study of ozone and carbon monoxide at the summit of mount Tai (1534m a.s.l.) in central-eastern China. *Atmospheric Environment*, *39*(26), 4779–4791. https://doi.org/10.1016/j.atmosenv.2005.04.030

Gaudel, A., Cooper, O. R., Ancellet, G., Barret, B., Boynard, A., Burrows, J. P., et al. (2018). Tropospheric Ozone Assessment Report: Present-day distribution and trends of tropospheric ozone relevant to climate and global atmospheric chemistry model evaluation. *Elementa: Science of the Anthropocene*, *6*, 39. https://doi.org/10.1525/elementa.291

Gu, R., Zheng, P., Chen, T., Dong, C., Wang, Y., Liu, Y., et al. (2020). Atmospheric nitrous acid (HONO) at a rural coastal site in North China: Seasonal variations and effects of biomass burning. *Atmospheric Environment*, *229*, 117429. https://doi.org/10.1016/j.atmosenv.2020.11742

Hayman, G. D. (1997). *Effects of pollution control on UV exposure. AEA Technology Final Report prepared for the Department of Health and Contract 121/6377*. Oxfordshire, UK: AEA Technology.

Hough, A. M., & Derwent, R. G. (1987). Computer modeling studies of the distribution of photochemical ozone production between different hydrocarbons. *Atmospheric Environment*, *21*(9), 2015–2033. https://doi.org/10.1016/0004-6981(87)90163-6

IPCC. (2013). *Climate change 2013: The physical science basis. Contribution of working group I to the fifth assessment Report of the intergovernmental Panel on climate change 1535*. Cambridge, UK; New York, NY: Cambridge University Press.

Jenkin, M. E., Saunders, S. M., Wagner, V., & Pilling, M. J. (2003). Protocol for the development of the Master Chemical Mechanism, MCM v3 (Part B): tropospheric degradation of aromatic volatile organic compounds. *Atmospheric Chemistry and Physics*, *3*(1), 181–193. https://doi.org/10.5194/acp-3-181-2003

Jian, Y., & Fu, T. M. (2014). Injection heights of springtime biomass-burning plumes over peninsular Southeast Asia and their impacts on long-range pollutant transport. *Atmospheric Chemistry and Physics*, *14*(8), 3977–3989. https://doi.org/10.5194/acp-14-3977-2014

Lefohn, A. S., Malley, C. S., Smith, L., Wells, B., Hazucha, M., Simon, H., et al. (2018). Tropospheric ozone assessment report: Global ozone metrics for climate change, human health, and crop/ecosystem research. *Elementa: Science of the Anthropocene*, *6*, 28. https://doi.org/10.1525/elementa.279

Lelieveld, J., Butler, T. M., Crowley, J. N., Dillon, T. J., Fischer, H., Ganzeveld, L., et al. (2008). Atmospheric oxidation capacity sustained by a tropical forest. *Nature*, *452*(7188), 737–740. https://doi.org/10.1038/nature06870

Li, H., Zhu, Y., Zhao, Y., Chen, T., Jiang, Y., Shan, Y., et al. (2020). Evaluation of the Performance of Low-Cost Air Quality Sensors at a High Mountain Station with Complex Meteorological Conditions. *Atmosphere*, *11*(2), 212. https://doi.org/10.3390/atmos11020212

Li, K., Jacob, D. J., Liao, H., Shen, L., Zhang, Q., & Bates, K. H. (2019). Anthropogenic drivers of 2013–2017 trends in summer surface ozone in China. *Proceedings of the National Academy of Sciences*, *116*(2), 422–427. https://doi.org/10.1073/pnas.1812168116

Li, M., Zhang, Q., Kurokawa, J. I., Woo, J. H., He, K., Lu, Z., et al. (2017). MIX: A mosaic Asian anthropogenic emission inventory under the international collaboration framework of the MICS-Asia and HTAP. *Atmospheric Chemistry and Physics*, *17*(2), 935–963. https://doi.org/10.5194/acp-17-935-2017

Li, M., Zhang, Q., Streets, D. G., He, K. B., Cheng, Y. F., Emmons, L. K., et al. (2014). Mapping Asian anthropogenic emissions of non-methane volatile organic compounds to multiple chemical mechanisms. *Atmospheric Chemistry and Physics*, *14*(11), 5617–5638. https://doi.org/10.5194/acp-14-5617-2014

Li, M., Zhang, Q., Zheng, B., Tong, D., Lei, Y., Liu, F., et al. (2019). Persistent growth of anthropogenic non-methane volatile organic compound (NMVOC) emissions in China during 1990–2017: Drivers, speciation and ozone formation potential. *Atmospheric Chemistry and Physics*, *19*(13), 8897–8913. https://doi.org/10.5194/acp-19-8897-2019

Li, Y., Lau, A. K.-H., Fung, J. C.-H., Zheng, J. Y., Zhong, L. J., & Louie, P. K. K. (2012). Ozone source apportionment (OSAT) to differentiate local regional and super-regional source contributions in the Pearl River Delta region, China. *Journal of Geophysical Research*, *117*(D15). https://doi.org/10.1029/2011jd017340

Ling, Z. H., Guo, H., Lam, S. H. M., Saunders, S. M., & Wang, T. (2014). Atmospheric photochemical reactivity and ozone production at two sites in Hong Kong: Application of a Master Chemical Mechanism–photochemical box model. *Journal of Geophysical Research: Atmospheres*, *119*(17), 10567–10582. https://doi.org/10.1002/2014jd021794

Liu, Y., Shao, M., Fu, L., Lu, S., Zeng, L., & Tang, D. (2008). Source profiles of volatile organic compounds (VOCs) measured in China: Part I. *Atmospheric Environment*, *42*(25), 6247–6260. https://doi.org/10.1016/j.atmosenv.2008.01.070

Liu, Y., Shao, M., Lu, S., Chang, C.-C., Wang, J.-L., & Fu, L. (2008). Source apportionment of ambient volatile organic compounds in the Pearl River Delta, China: Part II. *Atmospheric Environment*, *42*(25), 6261–6274. https://doi.org/10.1016/j.atmosenv.2008.02.027

Liu, Y., & Wang, T. (2020). Worsening urban ozone pollution in China from 2013 to 2017 – Part 2: The effects of emission changes and implications for multi-pollutant control. *Atmospheric Chemistry and Physics*, *2020*, 1–27. https://doi.org/10.5194/acp-2020-53

Lu, X., Hong, J., Zhang, L., Cooper, O. R., Schultz, M. G., Xu, X., et al. (2018). Severe surface ozone pollution in China: A global perspective. *Environmental Science and Technology Letters*, *5*(8), 487–494. https://doi.org/10.1021/acs.estlett.8b00366

Lu, X., Zhang, L., Wang, X., Gao, M., Li, K., Zhang, Y., et al. (2020). Rapid increases in warm-season surface ozone and resulting health impact in China since 2013. *Environmental Science and Technology Letters*, *7*(4), 240–247. https://doi.org/10.1021/acs.estlett.0c00171

Lyu, X., Wang, N., Guo, H., Xue, L., Jiang, F., Zeren, Y., et al. (2019). Causes of a continuous summertime O_3 pollution event in Jinan, a central city in the North China Plain. *Atmospheric Chemistry and Physics*, *19*(5), 3025–3042. https://doi.org/10.5194/acp-19-3025-2019

Lyu, X. P., Chen, N., Guo, H., Zhang, W. H., Wang, N., Wang, Y., & Liu, M. (2016). Ambient volatile organic compounds and their effect on ozone production in Wuhan, central China. *The Science of the Total Environment*, *541*, 200–209. https://doi.org/10.1016/j.scitotenv.2015.09.093

Ma, M., Gao, Y., Wang, Y., Zhang, S., Leung, L. R., Liu, C., et al. (2019). Substantial ozone enhancement over the North China Plain from increased biogenic emissions due to heat waves and land cover in summer 2017. *Atmospheric Chemistry and Physics*, *19*(19), 12195–12207. https://doi.org/10.5194/acp-19-12195-2019

Monks, P. S., Archibald, A. T., Colette, A., Cooper, O., Coyle, M., Derwent, R., et al. (2015). Tropospheric ozone and its precursors from the urban to the global scale from air quality to short-lived climate forcer. *Atmospheric Chemistry and Physics*, *15*(15), 8889–8973. https://doi.org/10.5194/acp-15-8889-2015

Saunders, S. M., Jenkin, M. E., Derwent, R. G., & Pilling, M. J. (2003). Protocol for the development of the Master Chemical Mechanism, MCM v3 (Part A): tropospheric degradation of non-aromatic volatile organic compounds. *Atmospheric Chemistry and Physics*, *3*(1), 161–180. https://doi.org/10.5194/acp-3-161-2003

Schroeder, J. R., Crawford, J. H., Ahn, J. Y., Chang, L., Fried, A., Walega, J., et al. (2020). Observation-based modeling of ozone chemistry in the Seoul metropolitan area during the Korea-United States Air Quality Study (KORUS-AQ). *Elementa: Science of the Anthropocene*, *8*, 3. https://doi.org/10.1525/elementa.400

Simon, H., Beck, L., Bhave, P. V., Divita, F., Hsu, Y., Luecken, D., et al. (2010). The development and uses of EPA's SPECIATE database. *Atmospheric Pollution Research*, *1*(4), 196–206. https://doi.org/10.5094/APR.2010.026

Sindelarova, K., Granier, C., Bouarar, I., Guenther, A., Tilmes, S., Stavrakou, T., et al. (2014). Global data set of biogenic VOC emissions calculated by the MEGAN model over the last 30 years. *Atmospheric Chemistry and Physics*, *14*(17), 9317–9341. https://doi.org/10.5194/acp-14-9317-2014

Sun, J., Li, Z., Xue, L., Wang, T., Wang, X., Gao, J., et al. (2018). Summertime C_1-C_5 alkyl nitrates over Beijing, northern China: Spatial distribution, regional transport, and formation mechanisms. *Atmospheric Research*, *204*, 102–109. https://doi.org/10.1016/j.atmosres.2018.01.014

Sun, L., Xue, L., Wang, T., Gao, J., Ding, A., Cooper, O. R., et al. (2016). Significant increase of summertime ozone at Mount Tai in Central Eastern China. *Atmospheric Chemistry and Physics*, *16*(16), 10637–10650. https://doi.org/10.5194/acp-16-10637-2016

Sun, L., Xue, L., Wang, Y., Li, L., Lin, J., Ni, R., et al. (2019). Impacts of meteorology and emissions on summertime surface ozone increases over central eastern China between 2003 and 2015. *Atmospheric Chemistry and Physics*, *19*(3), 1455–1469. https://doi.org/10.5194/acp-19-1455-2019

Tarasick, D. W., Carey-Smith, T. K., Hocking, W. K., Moeini, O., He, H., Liu, J., et al. (2019). Quantifying stratosphere-troposphere transport of ozone using balloon-borne ozonesondes, radar windprofilers and trajectory models. *Atmospheric Environment*, *198*, 496–509. https://doi.org/10.1016/j.atmosenv.2018.10.040

Tsai, S. M., Zhang, J., Smith, K. R., Ma, Y., Rasmussen, R. A., & Khalil, M. A. K. (2003). Characterization of non-methane hydrocarbons emitted from various cookstoves used in China. *Environmental Science & Technology*, *37*(13), 2869–2877. https://doi.org/10.1021/es026232a

USEPA. (2007). *USEPA: Guidance on the use of models and other analyses for demonstrating attainment of air quality goals for ozone, $PM_{2.5}$ and regional haze, EPA-454/B-07e002*. NC: United States Environmental Protection Agency.

Wang, R., Xu, X., Jia, S., Ma, R., Ran, L., Deng, Z., et al. (2017). Lower tropospheric distributions of O_3 and aerosol over Raoyang, a rural site in the North China Plain. *Atmospheric Chemistry and Physics*, *17*(6), 3891–3903. https://doi.org/10.5194/acp-17-3891-2017

Wang, S., Wei, W., Du, L., Li, G., & Hao, J. (2009). Characteristics of gaseous pollutants from biofuel-stoves in rural China. *Atmospheric Environment*, *43*(27), 4148–4154. https://doi.org/10.1016/j.atmosenv.2009.05.040

Wang, T., Dai, J., Lam, K. S., Nan Poon, C., & Brasseur, G. P. (2019). Twenty-five years of lower tropospheric ozone observations in Tropical East Asia: The influence of emissions and weather patterns. *Geophysical Research Letters*, *46*(20), 11463–11470. https://doi.org/10.1029/2019gl084459

Wang, T., Ding, A., Gao, J., & Wu, W. S. (2006). Strong ozone production in urban plumes from Beijing, China. *Geophysical Research Letters*, *33*(21). https://doi.org/10.1029/2006gl027689

Wang, T., Wei, X. L., Ding, A. J., Poon, C. N., Lam, K. S., Li, Y. S., et al. (2009). Increasing surface ozone concentrations in the background atmosphere of Southern China, 1994–2007. *Atmospheric Chemistry and Physics*, *9*(16), 6217–6227. https://doi.org/10.5194/acp-9-6217-2009

Wang, T., Xue, L., Brimblecombe, P., Lam, Y. F., Li, L., & Zhang, L. (2017). Ozone pollution in China: A review of concentrations, meteorological influences, chemical precursors, and effects. *The Science of the Total Environment*, *575*, 1582–1596. https://doi.org/10.1016/j.scitotenv.2016.10.081

Wei, W., lv, Z., Cheng, S., Wang, L., Ji, D., Zhou, Y., et al. (2015). Characterizing ozone pollution in a petrochemical industrial area in Beijing, China: A case study using a chemical reaction model. *Environmental Monitoring and Assessment*, *187*(6), 377. https://doi.org/10.1007/s10661-015-4620-5

Xiao, X., Cohan, D. S., Byun, D. W., & Ngan, F. (2010). Highly nonlinear ozone formation in the Houston region and implications for emission controls. *Journal of Geophysical Research: Atmospheres*, *115*(D23). https://doi.org/10.1029/2010jd014435

Xing, C., Liu, C., Wang, S., Chan, K. L., Gao, Y., Huang, X., et al. (2017). Observations of the vertical distributions of summertime atmospheric pollutants and the corresponding ozone production in Shanghai, China. *Atmospheric Chemistry and Physics*, *17*(23), 14275–14289. https://doi.org/10.5194/acp-17-14275-2017

Xing, J., Wang, S. X., Jang, C., Zhu, Y., & Hao, J. M. (2011). Nonlinear response of ozone to precursor emission changes in China: A modeling study using response surface methodology. *Atmospheric Chemistry and Physics*, *11*(10), 5027–5044. https://doi.org/10.5194/acp-11-5027-2011

Xu, X., Lin, W., Xu, W., Jin, J., Wang, Y., Zhang, G., et al. (2020). Long-term changes of regional ozone in China: Implications for human health and ecosystem impacts. *Elementa: Science of the Anthropocene*, *8*(1), 13. https://doi.org/10.1525/journal.elementa.409

Xue, L., Gu, R., Wang, T., Wang, X., Saunders, S., Blake, D., et al. (2016). Oxidative capacity and radical chemistry in the polluted atmosphere of Hong Kong and Pearl River Delta region: Analysis of a severe photochemical smog episode. *Atmospheric Chemistry and Physics*, *16*(15), 9891–9903. https://doi.org/10.5194/acp-16-9891-2016

Xue, L., Wang, T., Gao, J., Ding, A. J., Zhou, X. H., Blake, D. R., et al. (2014). Ground-level ozone in four Chinese cities: Precursors, regional transport and heterogeneous processes. *Atmospheric Chemistry and Physics*, *14*(23), 13175–13188. https://doi.org/10.5194/acp-14-13175-2014

Xue, L., Wang, T., Louie, P. K. K., Luk, C. W. Y., Blake, D. R., & Xu, Z. (2014). Increasing external effects negate local efforts to control ozone air pollution: A case study of Hong Kong and implications for other Chinese cities. *Environmental Science & Technology*, *48*(18), 10769–10775. https://doi.org/10.1021/es503278g

Yang, W., Chen, H., Wang, W., Wu, J., Li, J., Wang, Z., et al. (2019). Modeling study of ozone source apportionment over the Pearl River Delta in 2015. *Environmental Pollution*, *253*, 393–402. https://doi.org/10.1016/j.envpol.2019.06.091

Yuan, B., Shao, M., Lu, S., & Wang, B. (2010). Source profiles of volatile organic compounds associated with solvent use in Beijing, China. *Atmospheric Environment*, *44*(15), 1919–1926. https://doi.org/10.1016/j.atmosenv.2010.02.014

Zhang, L., Brook, J. R., & Vet, R. (2003). A revised parameterization for gaseous dry deposition in air-quality models. *Atmospheric Chemistry and Physics*, *3*(6), 2067–2082. https://doi.org/10.5194/acp-3-2067-2003

Zhang, Y., Ding, A., Mao, H., Nie, W., Zhou, D., Liu, L., et al. (2016). Impact of synoptic weather patterns and inter-decadal climate variability on air quality in the North China Plain during 1980–2013. *Atmospheric Environment*, *124*, 119–128. https://doi.org/10.1016/j.atmosenv.2015.05.063

Zheng, B., Tong, D., Li, M., Liu, F., Hong, C., Geng, G., et al. (2018). Trends in China's anthropogenic emissions since 2010 as the consequence of clean air actions. *Atmospheric Chemistry and Physics*, *18*(19), 14095–14111. https://doi.org/10.5194/acp-18-14095-2018

Zheng, J., Shao, M., Che, W., Zhang, L., Zhong, L., Zhang, Y., & Streets, D. (2009). Speciated VOC Emission Inventory and Spatial Patterns of Ozone Formation Potential in the Pearl River Delta, China. *Environmental Science & Technology*, *43*(22), 8580–8586. https://doi.org/10.1021/es901688e

Zhu, X., Ma, Z., Qiu, Y., Liu, H., Liu, Q., & Yin, X. (2020). An evaluation of the interaction of morning residual layer ozone and mixing layer ozone in rural areas of the North China Plain. *Atmospheric Research*, *236*, 104788. https://doi.org/10.1016/j.atmosres.2019.104788

Zhu, Y., Yang, L., Kawamura, K., Chen, J., Ono, K., Wang, X., et al. (2017). Contributions and source identification of biogenic and anthropogenic hydrocarbons to secondary organic aerosols at Mt. Tai in 2014. *Environmental Pollution*, *220*, 863–872. https://doi.org/10.1016/j.envpol.2016.10.070

Zong, R., Yang, X., Wen, L., Xu, C., Zhu, Y., Chen, T., et al. (2018). Strong ozone production at a rural site in the North China Plain: Mixed effects of urban plumesand biogenic emissions. *Journal of Environmental Sciences*, *71*, 261–270. https://doi.org/10.1016/j.jes.2018.05.003